Marangoni convection at electrogenerated hydrogen bubbles

Yang, X.; Baczyzmalski, D.; Cierpk, C.; Mutschke, G.; Eckert, K.;

Originally published:

May 2018

Physical Chemistry Chemical Physics 20(2018)17, 11542-11548

DOI: https://doi.org/10.1039/c8cp01050a

PCCP

ROYAL SOCIETY OF CHEMISTRY

ARTICLE TYPE

Cite this: DOI: 10.1039/xxxxxxxxxx

Marangoni convection at electrogenerated hydrogen bubbles

Xuegeng Yang,[a,‡] Dominik Baczyzmalski,[b,‡] Christian Cierpka,[c] Gerd Mutschke,[a] and Kerstin Eckert [*,a,d]

Received Date
Accepted Date

DOI: 10.1039/xxxxxxxxxx

www.rsc.org/journalname

Electrolytic gas evolution is a fundamental phenomenon occurring in a large number of industrial applications. In these processes gas bubbles are formed at the electrode from a supersaturated solution. Since dissolved gases can change the surface tension, a gas concentration gradient may cause the surface tension to vary locally at the gas bubble. Surface tension gradients may also form due to temperature gradients generated by ohmic heating of the electrolyte. In both cases, the resulting shear stress can impose a convection in the electrolyte and the gas bubble (Marangoni effect). This phenomenon may influence the entire electrolytic gas evolution process, e.g., by an enhanced mass transfer. In this study, the first evidence of the Marangoni convection near growing hydrogen bubbles, generated by water electrolysis, is provided. Microscopic high speed imaging was applied to study the evolution of single hydrogen bubbles at a microelectrode. The convection near the interface of the growing bubble was measured by using a time-resolved Particle Tracking Velocimetry (PTV) technique. The results indicate a clear correlation between the magnitude of the Marangoni convection and the electric current.

The Marangoni effect refers to a mostly small-scale flow driven by local inhomogeneities of surface tension σ, either caused by temperature (thermo-capillary flow) or by concentration gradients (soluto-capillary flow) of surface active substances (surfactants) at the interface. This phenomenon has a broad relevance ranging from chemical engineering and metallurgy to microfluidic phenomena, where it is responsible e.g. for the remarkable deposition patterns of the dispersed phase and the related variation of the evaporation rate of evaporating droplets[1,2] or the collective motion of the micromotors[3]. In chemical engineering, the change of the surface tension, σ, due variations in the concentration of surfactants, $d\sigma/dc\ \Delta c$, i.e., the forcing of the flow, is much larger than that caused by temperature changes, $d\sigma/dT\ \Delta T$. Significant progress has recently been achieved in understanding the complex convection patterns resulting from the strong nonlinearity introduced by the Marangoni effect[4–6]. A distinct feature consists in the formation of hierarchic cellular patterns in which small convection cells of first order, free of any further substructure, are embedded in larger cells of second order. Cell sizes up to 3rd order have been observed[7]. Furthermore, improved understanding of the influence of the Marangoni effect on the convective dynamics of autocatalytic chemical fronts has been obtained recently[8,9].

In contrast to plane interfaces, the pre-set length scale of bubbles and drops frequently hinders the formation of such hierarchic cellular structures, and mostly Marangoni cells of first order are formed. However, even at the lowest hierarchy level the impact of Marangoni convection was found to be significant as it was shown for rising bubbles or drops with mass transfer towards the continuous phase[10–12]. Also in subcooled pool boiling, thermal Marangoni convection has long been recognized as an important heat transfer mechanism[13–15]. The origin of this flow is the accumulation of noncondensable gas at the top of the bubble laying in the subcooled region. As a result, the partial pressure of the vapor is reduced, which in turn decreases the local saturation temperature from the top to the bottom of the vapor bubble[16].

However, comparable evidence of a Marangoni effect does not exist for the important class of electrogenerated bubbles. This is especially surprising considering the importance of nucleated gas bubbles and dissolved gases in electrolyzers[17,18] and photocatalytic reactors[19,20]. In particular, the hydrogen production through water electrolysis and its application as an energy carrier has now become increasingly relevant in view of the steadily growing application of renewable energies[21]. However, one ma-

[a] Helmholtz-Zentrum Dresden-Rossendorf (HZDR), 01314 Dresden, Germany.
[b] Institute of Fluid Mechanics and Aerodynamics, Universität der Bundeswehr München, 85577 Neubiberg, Germany.
[c] Institute of Thermodynamics and Fluid Mechanics, Technische Universität Ilmenau, 98684 Ilmenau, Germany.
[d] Institute of Process Engineering, Technische Universität Dresden, 01062 Dresden, Germany.
∗ kerstin.eckert@hzdr.de.
‡ These authors contributed equally to this work.

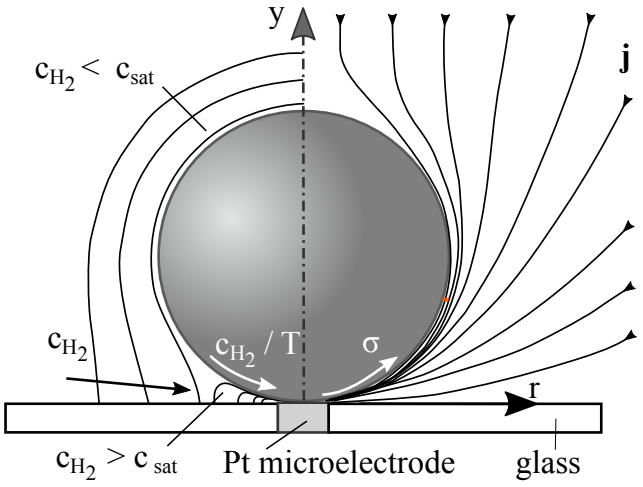

Fig. 1 Schematic distribution of the current density j and the hydrogen concentration c_{H_2} around the growing gas bubble based on previous simulations[27].

jor challenge for the establishment of water electrolysis on an industrial scale is its relatively low efficiency. A significant part of the losses is caused by the formation of hydrogen gas bubbles on the electrode surface[22]. Therefore, a better insight into the bubble nucleation, growth and detachment mechanisms, including surface tension-driven flows, is still necessary. For detailed experimental investigations, microelectrodes are especially attractive as the nucleation site is spatially constrained[23–30].

The nucleation and growth of the electrolytic gas bubbles takes place within the the concentration boundary layer (Nernst layer) of the supersaturated gas produced at the electrode[31]. The left side of Fig. 1 shows a schematic distribution of the concentration of the dissolved hydrogen near a gas bubble growing at a microelectrode according to previous numerical results[27]. Since some dissolved gases such as hydrogen and oxygen are known to alter the surface tension[32], it was suspected earlier that the inhomogeneous hydrogen concentration causes a gradient of the surface tension along the bubble interface[33]. However, in thermodynamic equilibrium of evaporation and dissolution at the interface, the concentration of dissolved hydrogen equals the saturation concentration defined by Henry's law. A quantitative description of the solutal hydrogen effect resulting from deviations of equilibrium or further effects is missing so far. Additionally, at microelectrodes investigated here, local ohmic heating due to the high current density near the bubble foot is likely to impose a temperature gradient along the bubble interface (Fig. 1, right). Both, the solutal and the thermal effect, may give rise to a Marangoni convection according to the shear stress condition at the gas-liquid interface

$$\mathbf{t}\cdot\tau_{\mathbf{e}}\cdot\mathbf{n}-\mathbf{t}\cdot\tau_{\mathbf{g}}\cdot\mathbf{n}=\mathbf{t}\cdot\nabla\sigma. \quad (1)$$

In Eq. (1), τ_e and τ_g denote the viscous stress tensor of electrolyte and gas, and $\mathbf{t}$ and $\mathbf{n}$ refer to the tangential and the normal vector. Thus, the shear stress, $\nabla\sigma$, generated induces a convection on both the electrolyte and gas side, which is directed from the region of low surface tension at the electrode torwards higher surface tension farther away from the electrode. Indeed, it was speculated by Lubetkin[33] that the solutal Marangoni effect is the origin of several puzzling and unresolved problems of electrolysis. Among these are the sudden jump-off of the bubble from the electrode and its return to it[34], the radial coalescence of bubbles[35,36] or the oscillatory tracks of microbubbles rising near vertical electrodes[37]. Moreover, the Marangoni force may retard the detachment of the bubble from the electrode, which reduces the active electrode area available for electrochemical reactions and causes undesired energy losses in water electrolysis. Despite these important unresolved issues which might be caused by the Marangoni effect, a direct proof of its existence during the electrolytic gas evolution is still missing. Using a favorable range of electrode potentials together with advanced particle tracking algorithms, we demonstrate the existence of the Marangoni flow at single hydrogen bubbles growing at a microelectrode, and analyze its dynamics, which are strongly correlated with the faradaic current.

Single hydrogen bubbles were generated in a glass cell with a three-electrode system under potentiostatic conditions[27]. A platinum wire with a diameter of 100 μm was used as the working electrode (Fig. 1). This microelectrode was manufactured by embedding the Pt wire in a glass tube of 6 mm outer diameter, which formed the bottom of the electrochemical cell. The electrolyte was a 1 M H_2SO_4 solution. All electrode potentials refer to mercury/mercurous sulphate electrode (MSE, 650 mV vs. standard hydrogen electrode (SHE)). As in previous works[26–29], measurements of the electric current and microscopic high speed imaging were employed to study the evolution of the hydrogen bubble and the flow field in its vicinity. A diffuse LED light source was used for the background illumination. The images were recorded at a frame rate of 500 fps with a magnification of $M \approx 6$, resulting in a resolution of approximately 0.43 pixel/μm. In difference to Yang et. al[26], a broader range of potentials (-1.2 V$\ldots-10$ V) was applied at the working electrode for time periods of 60 seconds. Under these conditions, considerably larger hydrogen bubbles ($\sim$ 1 mm) can be produced compared to all previous studies without any electrochemical side reaction. The advantage of this approach is that the larger bubbles size gives rise to larger flow structures, which enables accurate measurements of the Marangoni convection at the foot of the growing bubble.

Polystyrene (PS) tracer particles with a diameter of 1 μm were added to the electrolyte to measure the convection around the growing bubble, especially the Marangoni flow near the gas-liquid interface. Since the depth of field of the imaged particles is very small compared to the bubble size, two-dimensional measurements in the center plane of the bubble are possible with this approach. The flow measurements were performed by means of Particle Tracking Velocimetry (PTV), a technique in which the motion of individual particles is tracked to reconstruct the flow field. In contrast to correlation-based methods, i.e. Particle Image Velocimetry (PIV), PTV enables unbiased measurements in regions of high velocity gradients[38] as is the case here. Common preprocessing steps such as a background image subtraction and additional image filters were applied to remove background inhomogeneities and image noise, thus allowing for a reliable detection

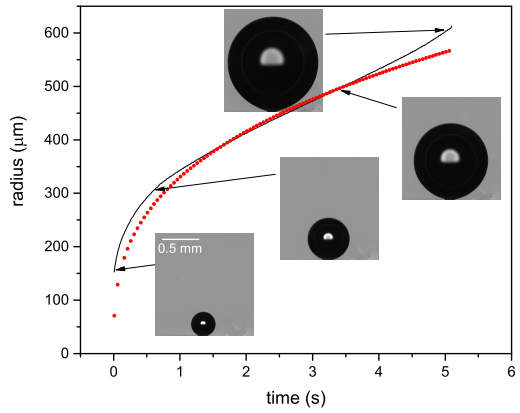

Fig. 2 The growth of a large H_2 bubble at E = -8V as a function of time. The insets show bubble images at different times indicated by the arrows. The red dotted line corresponds to a growth $R(t) \propto t^{1/3}$, in detail $R = 330\mu m \times t^{1/3}$ (t is time in second).

of individual particle images. A time-resolved tracking algorithm was applied to identify corresponding particle image pairs in successive frames. In contrast to standard tracking techniques, this algorithm uses a predictor for the particle displacement based on previous times steps. This feature can be regarded as a local adaptive histogramm filter and was crucial for a reliable measurement as the fluid experiences an extreme acceleration near the interface. Finally, a higher order velocity estimation and vector reallocation based on a local polynomial fit of the particle trajectory was applied to further improve the measurement accuracy[39].

The evolution of the bubble size until its detachment is exemplified in Fig. 2 for a cathodic potential of -8V. The inserts display the bubble images at different times during the bubble growth. With exception of the intial and the last phase, the bubble growth follows the $R(t) \propto t^{1/3}$ law [23,26,40], which is characteristic for high current densities at the surface, particularly in the case of microelectrodes. In this regime, almost the entire hydrogen generated at the electrode surface diffuses directly into the bubble at its foot due to the high local supersaturation level. Deviations from this growth law in the form of an accelerated growth occur in the late phase, which can be attributed to a strong increase of the cathodic current. At about 5 seconds after nucleation the bubble detaches from the surface at a diameter of 1.2 mm, at which point the buoyancy exceeds the forces keeping the bubble attached to the electrode surface. The detachment of the bubble is immediately followed by the nucleation of a new bubble at the microelectrode.

The transients of the current density, given by the current divided by the area of the microelectrode are plotted in Fig.3a over the duration of the experiment at different potentials. The current density shows a periodic behavior at all potentials where each period comprises growth and detachment of a single bubble. The duration of these periods and the final size of the bubble increases with the potential as shown in Fig.3b. After detachment of the bubble from the electrode, the new bubble is still small, hence surface coverage is minimum. As a result, the current density attains its peak current, j_p, which increases with increasing cathodic potential, see Fig. 3b. With growing bubble size, a large part of the electrode is blocked, which results in a plateau of the current density over almost 80% of the bubble lifetime. The plateau current, j_{pl}, which is also shown in Fig. 3b, is nearly independent of the potential applied as the surface coverage is almost 100%.

It is known that surface-active contaminations in the electrolyte influence growth and departure diameter of the bubble[23]. To exclude any surface-active behavior of the polystyrene tracer particles which were added at low concentration to the electrolyte for the PIV measurements, a large part of the current transients was repeatedly measured in the presence of tracer particles. Fig. 3b shows that the differences in the measured quantities are small, which clearly indicates that the dynamics remain unchanged by the addition of the tracer particles. No attachment of these tracers onto the bubble interface were observed during the experiments.

The temporal evolution of the flow field around a growing bubble is shown in Fig. 4 for an electrode potential of -8 V. Qualitatively the flow fields display the same features, irrespective of the electrode potentials in the studied range from -1.2 V to -10 V. However, for a detailed discussion and quantitative comparison between the different cases, measurements at higher electrode potentials (-3 V, -4 V, -8V and -10 V) were chosen. In this potential range, the bubbles become relatively large and show long lifetimes, see Fig. 3. Thus, also the corresponding flow structures get larger which makes it easier to properly resolve the shear flow close to the interface.

Fig. 4 plots the particle trajectories and the corresponding velocities at different stages of the bubble growth. On the upper side of the bubble the electrolyte is simply displaced by the bubble growth with a velocity of about $u_y \approx 0.5$ mm/s. Close to the electrode at the foot of the bubble a much stronger convection can be observed. It reaches velocities of up to $u \approx 20 - 30$ mm/s directly at the gas-liquid interface (Fig. 4d) and falls rapidly to zero within a distance of less than 60 μm from the interface. This flow is directed parallel to the interface and points away from the electrode. By continuity, a larger vortex is formed to replenish the electrolyte that is displaced by the convection. The fluid velocities decrease to zero directly at the bottom wall and the electrode to satisfy the no-slip condition. Moreover, both the size of the vortex and the fluid velocities increase during the final growth stages as can be seen from Fig. 4. The phenomenology of this convection with the velocity maximum at the bubble surface shows the clear features of a Marangoni convection. Considering the three-dimensional configuration, Fig. 4 represents two-dimensional cuts through an axisymmetric toroidal Marangoni vortex around the hydrogen bubble.

To further analyze its temporal evolution, it is useful to define a characteristic velocity close to the interface. However, only a few data points are available in immediate vicinity of the interface due to the difficulty to properly measure the extreme fluid acceleration in this region. Therefore, the velocity data at a distance of about $23 - 46$ μm ($10 - 20$ pixel) away from the bubble interface within small time intervals of $\Delta t = 0.1$ s is considered here instead. The spatial distribution of the data in this thin shear layer along

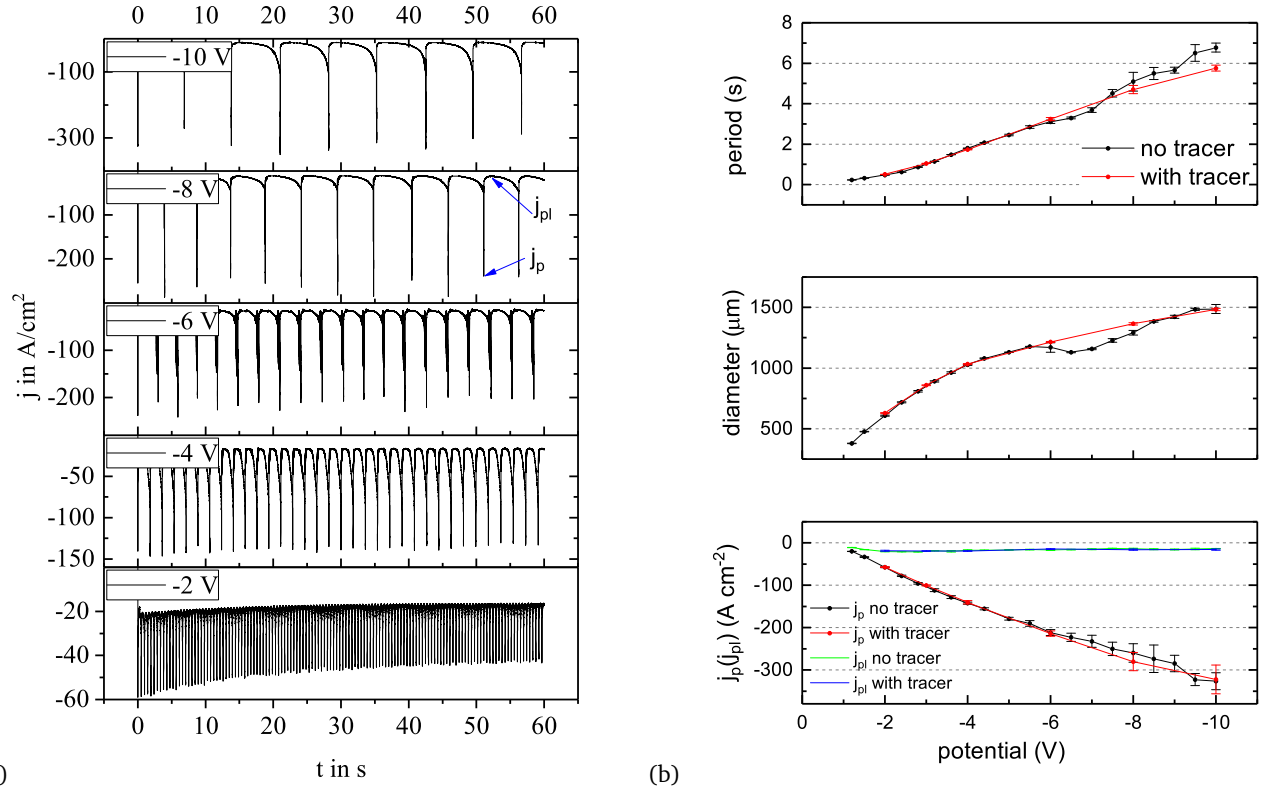

Fig. 3 (a) Transients of the current density averaged over the area of the microelectrode at different cathodic potentials within 60 seconds of bubble generation. (b) Period of the current oscillations, final size of the bubbles, peak current j_p and plateau current j_{pl} density as a function of the potential applied. Red symbols refer to measurement with PS tracer particles. All values are averaged over 5 measurements, each lasting for 60 s. Error bars show the standard deviation.

the interface was approximated by a second order polynomial, the maximum of which was used to characterize the development of the convection. The evolution of this characteristic Marangoni velocity during one bubble cycle at different potentials and the corresponding electric current density are shown in Fig. 5. Both quantities have been normalized according to their corresponding value at the plateau current density j_{pl} for a better comparision between the different potentials. For all potentials investigated it is clearly evident that the magnitude of the Marangoni convection is directly related to the electric current density j.

The convection pattern in Fig. 4 displays the maximum of the velocity at the interface, thereby differing from that of a buoyancy-driven flow, caused by changes in density due to variations of temperature and concentration in the electrolyte. The acceleration of fluid volume from the buoyant boundary layers leads to a velocity maximum in the bulk liquid, hence separated from the boundary layer. The distinct velocity maximum at the interface, therefore, points to a forcing by the Marangoni effect. Fig. 5 shows a clear correlation between the characteristic velocity of the Marangoni flow near the interface and the current density: the higher the current density the larger is the velocity. As already anticipated in the introduction, this enables both the soluto- and the thermocapillary effects to come into play as driving force. - The amount of hydrogen produced scales with the current according to Faraday's law, whereas the ohmic heat generated scales with the current squared.

To asses the respective impact of the soluto- vs. the thermocapillary effect we consider the ratio of the corresponding surface tension gradients:

$$\frac{(\nabla\sigma)_{\mathrm{sc}}}{(\nabla\sigma)_{\mathrm{tc}}} \approx \frac{\frac{\partial\sigma}{\partial c_{\mathrm{H_2}}}\frac{\Delta c_{\mathrm{H_2}}}{\delta_{\mathrm{c}}}}{\frac{\partial\sigma}{\partial T}\frac{\Delta T}{\delta_{\mathrm{th}}}} \approx \frac{\frac{\partial\sigma}{\partial c_{\mathrm{H_2}}}}{\frac{\partial\sigma}{\partial T}} \cdot \frac{\delta_{\mathrm{th}}}{\delta_{\mathrm{c}}} \cdot \frac{\Delta c_{\mathrm{H_2}}}{\Delta T} \qquad (2)$$

The first term of the rhs of Eq. (2) contains the dependencies of σ on concentration and temperature. For the latter we take that of water, $\frac{\partial\sigma}{\partial T} = -1.6\cdot10^{-4}\ \frac{\mathrm{N}}{\mathrm{m\,K}}$ [41] as a representative value. To estimate $\partial\sigma/\partial c_{\mathrm{H_2}}$ we use $\frac{\partial\sigma}{\partial p} = -2.5\cdot10^{-10}\frac{\mathrm{N}}{\mathrm{mPa}}$ (Ref.[32]). The partial hydrogen pressure, p, in the bubble is related to the concentration of dissolved hydrogen via Henry's law, $c_{\mathrm{H_2}} = K_H\,p$, where the Henry constant, K_H, is given by $K_H = 7.8\cdot10^{-6}\frac{\mathrm{mol}}{\mathrm{m^3\,Pa}}$ (Ref.[42,43]). As a result we obtain

$\frac{\partial\sigma}{\partial c_{\mathrm{H_2}}} = \frac{1}{K_H}\frac{\partial\sigma}{\partial p} = -3.2\cdot10^{-5}\frac{\mathrm{N\ m^3}}{\mathrm{m\ mol}}$.

The ratio between thermal and concentration boundary layer, $\delta_{\mathrm{th}}/\delta_{\mathrm{c}}$, in the second term of the rhs of Eq. (2) depends on the Reynolds number of the Marangoni convection and on the coupling between the three fields, u, c and T. The Reynolds number, $Re = uR/\nu$, amounts to $O(Re)\sim 3$. Hence the flow is laminar. We take the scaling for a laminar flow over an electrode or a heated plate for which holds $\delta_{\mathrm{th}}/\delta_{\mathrm{u}} \sim Pr^{-1/2}$ (Ref. [44]) and $\delta_{\mathrm{c}}/\delta_{\mathrm{u}} \sim Sc^{-1/2}$ (Ref.[45]), respectively, as a rough estimate where Pr and Sc refer

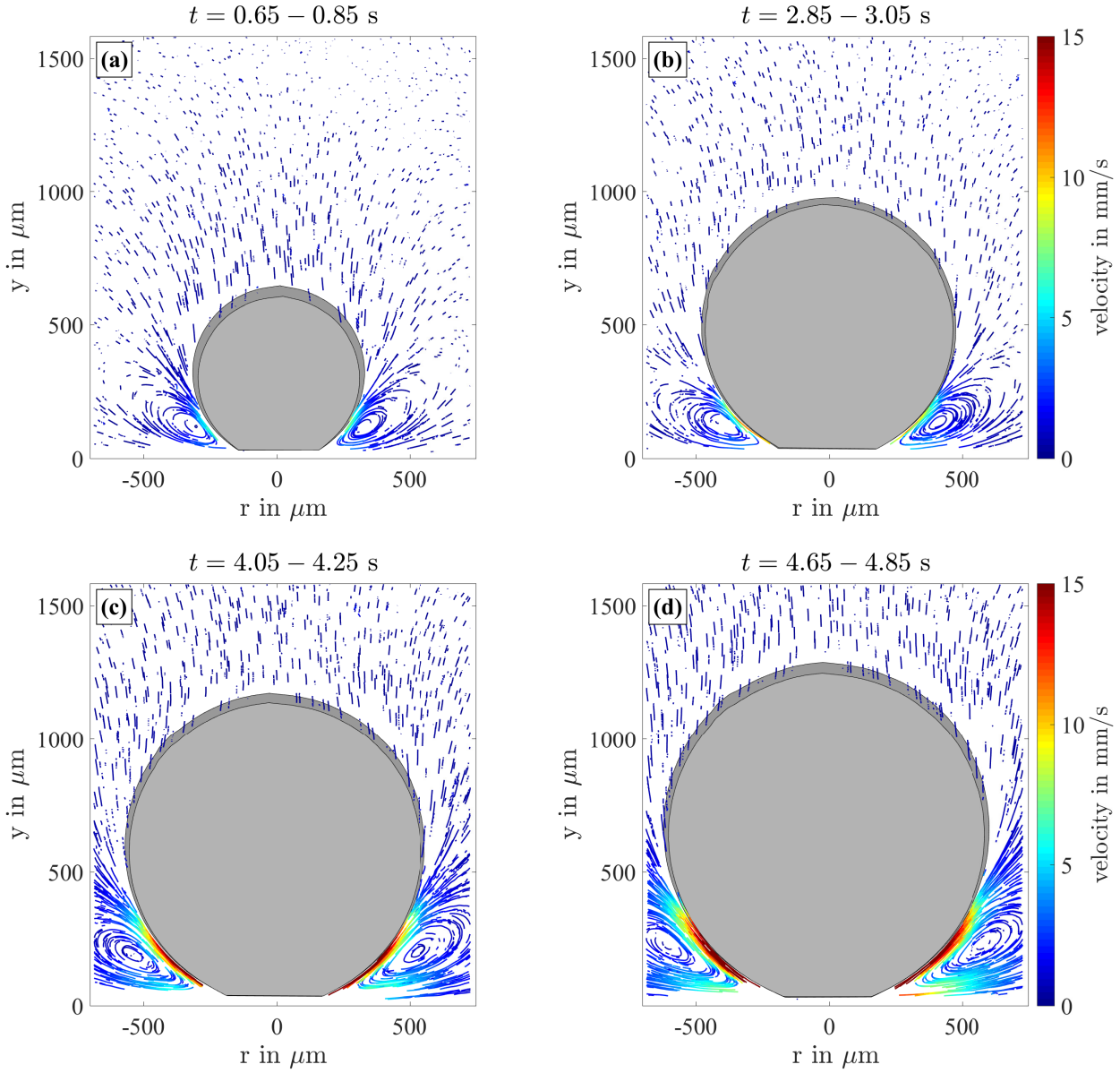

Fig. 4 Particle trajectories and corresponding velocities around the growing bubble for different growth stages at a potential of -8 V. For the sake of better visibility, the velocity limit displayed at the color scale was set to about half of the maximum value observed.

to the Prandtl and Schmidt numbers. For the given electrolyte they amount to $Pr \sim 10^2$ and $Sc \sim 10^3$ so that $\delta_{\mathrm{th}}/\delta_{\mathrm{c}} \sim 10$ is obtained, i.e. the thermal boundary layer is by a factor of ten times larger than the concentration boundary layer.

To approximate the third term, $\Delta c_{\mathrm{H_2}}/\Delta T$, we take the concentration drop, Δc_{H_2}, across δ_{c} in a conservative estimation equal to the saturation concentration $c^s_{H_2}$ of $\mathrm{H_2}$ ($c^s_{H_2} = 0.75 \times 10^{-3}$ mol/l at 28°C, Ref.[46]). Concerning the temperature drop, a $\Delta T \leq 10$ K can be considered as a safe approximation for lower values of the electric potential, which is supported by measurements with a thermocouple instead of a Pt electrode[47]. Inserting all estimated quantities into Eq. 2 we obtain $\frac{(\nabla\sigma)_{\mathrm{sc}}}{(\nabla\sigma)_{\mathrm{tc}}} \approx 0.2$. Having in mind that the actual supersaturation in the present setup might be considerably underestimated (in Ref.[26], a value of $c_{H_2} \sim 0.29$ mol/l is mentioned), this result signals that the soluto- and the thermocapillary contribution can be of the same order of magnitude.

Next, the characteristic velocity scale, u_M, for the Marangoni convection is estimated. Equation (1) can be simplified to $\mathbf{t} \cdot \tau_e \cdot \mathbf{n} = \mu_e \frac{\partial u_M}{\partial l_n} \sim \left|\frac{\partial \sigma}{\partial T}\right| \frac{\Delta T}{\delta_{||}}$, based on two arguments: First, the circulation inside the hydrogen bubble can be neglected because for the ratio of dynamic viscosities between electrolyte (subscript e) and gas holds $\mu_e/\mu_g \gg 1$ with $\mu_e \approx 1.2 \cdot 10^{-3}$ kg/(m s)[48]. Second, the thermocapillary effect is roughly of the same order of magnitude as the soluto-capillary one. The distance normal the bubbles surface across which the velocity drops down to zero can be estimated as $l_n \sim R/10$. The surface-parallel length, $\delta_{||}$, along which the temperature drop $\Delta T \leq 10$ K[47] occurs can be estimated to $\delta_{||} \sim 2 \cdot R$. Using these values we obtain $u_M \leq 66$ mm/s which is of the same order as the maximum velocity observed in the experiment.

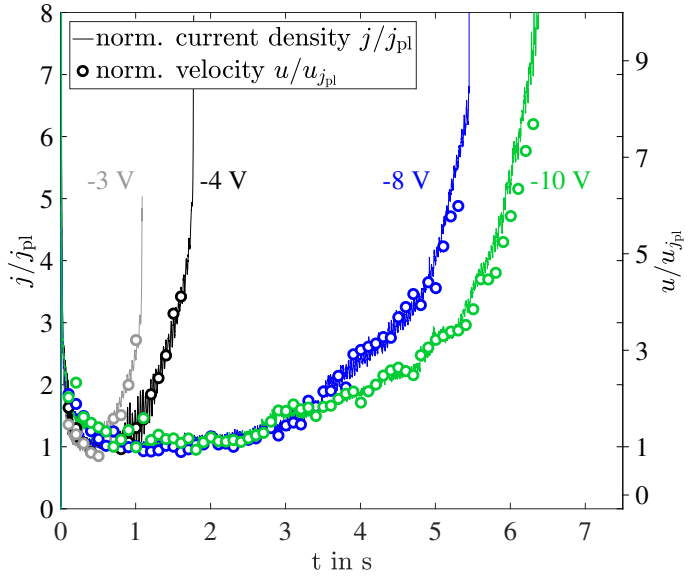

Fig. 5 Comparison of the near-interface velocity associated with the Marangoni convection vs. the current transient during one bubble cycle at different potentials. The velocity corresponds to the maximum velocity at a distance of about $23-46\ \mu$m $(10-20$ pixel) normal to the bubble interface within time intervals of $\Delta t = 0.1$ s. Both the current and the velocity are normalized according to their value at the plateau current. Normalization values: $u_{j_{\mathrm{pl}}} \approx \{1.9;\ 2.1;\ 2.3;\ 2.7\}$ mm/s and $j_{\mathrm{pl}} \approx \{-20.4;\ -17.8;\ -12.7;\ -12.7\}$ A/cm^2 for the potentials of $E = \{-3;\ -4;\ -8;\ -10\}$ V.

Although the experimental results and the theoretical analysis clearly demonstrate the existence of a Marangoni vortex at electrogenerated hydrogen bubbles, the clarification of the major driving mechanism remains a scientific challenge. Indeed, the forcing by ohmic heating and the gradient of dissolved hydrogen are intricately coupled in the wedge-like electrolyte volume at the foot of the hydrogen bubble. The transport of species along the interface is dominated by the Marangoni convection only, whereas transport of heat may also be influenced by diffusion since the Peclet number, referring to the ratio of convective to diffusive transport equals $Pe_T \sim 1$, and the ratio between thermal to mass diffusivity, D_T/D_c is ~ 100[31,48]. Moreover, hydrogen is only produced at the electrode surface, whereas heat is mainly generated in the electrolyte surrounding the bubble, although its maximum will also occur near the electrode due to the high current density (Fig. 1). An improved understanding requires both a dedicated strategy for a discrimination between soluto- and thermocapillary effect and further improvements in the spatial and temporal resolution to resolve the strong velocity gradient at the interface.

Furthermore, our study addresses two conceptional problems which deserve a more detailed attention. (i) The estimation of the solutal effect is based on the assumption that concentration gradients actually exist at the interface, which is not the case at thermodynamic equilibrium[33]. (ii) A fundamental problem of comparable importance as that of the surface tension of nanobubbles[49] concerns the influence of the electric charge of the bubble on the surface tension. Typically, the bubble carries a positive charge in the acidic range below the isoelectric point[50] due to the specific adsorption of protons at the bubble surface. However, due to the consumption of the protons in the reaction, also a strong gradient in the pH value exists in the electrolyte wedge at the bubble foot. One could infer to a spatially varying charge and hence electric potential distribution at the bubble surface, which might impact the surface tension via electrocapillary effects. Thus, the evidence brought about the existence of a Marangoni convection at electrogenerated hydrogen bubbles simultaneously rises important physico-chemical questions, and we hope to stimulate further research in this field.

Conflicts of interest

There are no conflicts of interest to declare.

Acknowledgements

K.E., C.C. and D.B. thank Deutsche Forschungsgemeinschaft for financial support in the frame of Ec201/4, SPP 1506 (Ec201/2-2) and CI 185/3. We are thankful to Margitta Uhlemann und Franziska Karnbach for fruitful discusssions and for providing the electrolytic cell.

Author contributions statement

X.Y. performed the experiments, D.B. and C.C. provided guidance with respect to the flow measurements, X.Y. and K.E. processed the electrochemical measurements, D.B and C.C. processed the image data, K.E., D.B., G.M. and X.Y. wrote the manuscript, all authors analyzed the data and reviewed the manuscript.

References

1 H. Hu and R. G. Larson, *The Journal of Physical Chemistry B*, 2006, **110**, 7090–7094.
2 V. Soulié, S. Karpitschka, F. Lequien, P. Prené, T. Zemb, H. Moehwald and H. Riegler, *Physical Chemistry Chemical Physics*, 2015, **17**, 22296–22303.
3 M. Manjare, F. Yang, R. Qiao and Y. Zhao, *The Journal of Physical Chemistry C*, 2015, **119**, 28361–28367.
4 K. Schwarzenberger, T. Köllner, H. Linde, T. Boeck, S. Odenbach and K. Eckert, *Advances in Colloid and Interface Science*, 2014, **206**, 344 – 371.
5 K. Schwarzenberger, S. Aland, H. Domnick, S. Odenbach and K. Eckert, *Colloids and Surfaces A: Physicochemical and Engineering Aspects*, 2015, **481**, 633–643.
6 T. Köllner, K. Schwarzenberger, K. Eckert and T. Boeck, *Journal of Fluid Mechanics*, 2016, **791**, R4.
7 H. Linde and E. Schwarz, *Zeitschrift für physikalische Chemie*, 1963, **224**, 331–352.
8 D. Horváth, M. A. Budroni, P. Bába, L. Rongy, A. De Wit, K. Eckert, M. J. Hauser and Á. Tóth, *Physical Chemistry Chemical Physics*, 2014, **16**, 26279–26287.
9 K. Eckert, L. Rongy and A. De Wit, *Physical Chemistry Chemical Physics*, 2012, **14**, 7337–7345.
10 R. F. Engberg, M. Wegener and E. Y. Kenig, *Chemical Engineering Science*, 2014, **116**, 208–222.

11 J. Chen, C. Yang and Z.-S. Mao, *The European Physical Journal Special Topics*, 2015, **224**, 389–399.

12 M. Wegener, *International Journal of Heat and Mass Transfer*, 2014, **71**, 769–778.

13 J. Straub, *Experimental Thermal and Fluid Science*, 1994, **9**, 253–273.

14 S. Petrovic, T. Robinson and R. L. Judd, *International Journal of Heat and Mass Transfer*, 2004, **47**, 5115–5128.

15 V. K. Dhir, G. R. Warrier, E. Aktinol, D. Chao, J. Eggers, W. Sheredy and W. Booth, *Microgravity Science and Technology*, 2012, **24**, 307–325.

16 R. Marek and J. Straub, *International Journal of Heat and Mass Transfer*, 2001, **44**, 619–632.

17 D. Pletcher and X. Li, *International Journal of Hydrogen Energy*, 2011, **36**, 15089–15104.

18 D. Zhang and K. Zeng, *Industrial & Engineering Chemistry Research*, 2012, **51**, 13825–13832.

19 X. Chen, S. Shen, L. Guo and S. S. Mao, *Chemical Reviews*, 2010, **110**, 6503–6570.

20 X. Hu, Z. Cao, Y. Wang, S. Shen, L. Guo and J. Chen, *Electrochimica Acta*, 2016, **202**, 175–185.

21 A. Ursua, L. M. Gandia and P. Sanchis, *Proceedings of the IEEE*, 2012, **100**, 410–426.

22 J. Dukovic and C. W. Tobias, *Journal of the Electrochemical Society*, 1987, **134**, 331–343.

23 D. Fernández, P. Maurer, M. Martine, J. Coey and M. E. Möbius, *Langmuir*, 2014, **30**, 13065–13074.

24 D. Fernández, M. Martine, A. Meagher, M. E. Möbius and J. Coey, *Electrochemistry Communications*, 2012, **18**, 28–32.

25 L. Luo and H. S. White, *Langmuir*, 2013, **29**, 11169–11175.

26 X. Yang, F. Karnbach, M. Uhlemann, S. Odenbach and K. Eckert, *Langmuir*, 2015, **31**, 8184–8193.

27 F. Karnbach, X. Yang, G. Mutschke, J. Fröhlich, J. Eckert, A. Gebert, K. Tschulik, K. Eckert and M. Uhlemann, *The Journal of Physical Chemistry C*, 2016, **120**, 15137–15146.

28 D. Baczyzmalski, F. Karnbach, G. Mutschke, X. Yang, M. Uhlemann, K. Eckert and C. Cierpka, *Physical Review Fluids*, 2017, **2**, 093701.

29 D. Baczyzmalski, F. Karnbach, X. Yang, G. Mutschke, M. Uhlemann, K. Eckert and C. Cierpka, *Journal of The Electrochemical Society*, 2016, **163**, E248–E257.

30 H. Liu, L. Pan, H. Huang, Q. Qin, P. Li and J. Wen, *Journal of Electroanalytical Chemistry*, 2015, **754**, 22 – 29.

31 H. Vogt, *Electrochimica Acta*, 1980, **25**, 527 – 531.

32 R. Massoudi and A. King Jr, *The Journal of Physical Chemistry*, 1974, **78**, 2262–2266.

33 S. Lubetkin, *Electrochimica Acta*, 2002, **48**, 357–375.

34 D. E. Westerheide and J. Westwater, *AIChE Journal*, 1961, **7**, 357–362.

35 P. J. Sides and C. W. Tobias, *Journal of The Electrochemical Society*, 1985, **132**, 583–587.

36 S. A. Guelcher, Y. E. Solomentsev, P. J. Sides and J. L. Anderson, *Journal of the Electrochemical Society*, 1998, **145**, 1848–1855.

37 L. J. Janssen and J. Hoogland, *Electrochimica Acta*, 1970, **15**, 1013–1023.

38 C. J. Kähler, S. Scharnowski and C. Cierpka, *Experiments in Fluids*, 2012, **52**, 1641 – 1656.

39 C. Cierpka, B. Lütke and C. J. Kähler, *Experiments in Fluids*, 2013, **54**, 1533.

40 H. Verhaart, R. De Jonge and S. Van Stralen, *International Journal of Heat and Mass Transfer*, 1980, **23**, 293–299.

41 G. Vazquez, E. Alvarez and J. M. Navaza, *Journal of Chemical and Engineering Data*, 1995, **40**, 611–614.

42 R. Wiebe and V. Gaddy, *Journal of the American Chemical Society*, 1934, **56**, 76–79.

43 R. Sander, *Atmospheric Chemistry & Physics*, 2015, **15**, year.

44 A. Bejan, *Convection heat transfer*, John wiley & sons, 2013.

45 H. Wendt and G. Kreysa, *Electrochemical engineering: science and technology in chemical and other industries*, Springer Science & Business Media, 1999.

46 J. Glas and J. Westwater, *International Journal of Heat and Mass Transfer*, 1964, **7**, 1427–1443.

47 F. Karnbach, *PhD thesis*, TU Dresden, unpublished, 2018.

48 D. R. Lide, *CRC Handbook of Chemistry and Physics, 87th Edition*, CRC Press, 2006.

49 S. R. German, M. A. Edwards, Q. Chen and H. S. White, *Nano letters*, 2016, **16**, 6691–6694.

50 N. Brandon and G. Kelsall, *Journal of Applied Electrochemistry*, 1985, **15**, 475–484.